# Erythrocyte Membrane Is an Alternative Coating to Polyethylene Glycol for Prolonging the Circulation Lifetime of Gold Nanocages for Photothermal Therapy

Ji-Gang Piao,[†,‡,⊥] Limin Wang,[‡,⊥] Feng Gao,[‡,§] Ye-Zi You,[*,†,‡] Yujie Xiong,[*,‡] and Lihua Yang[*,†,‡]

[†]CAS Key Laboratory of Soft Matter Chemistry, [‡]School of Chemistry and Materials Science, [§]CAS Key Laboratory of Materials for Energy Conversion, University of Science and Technology of China, Hefei, Anhui 230026 China. [⊥]J.-G.P. and L.W. contributed equally.

ABSTRACT Gold nanocages (AuNCs), which have tunable near-infrared (NIR) absorption and intrinsically high photothermal conversion efficiency, have been actively investigated as photothermal conversion agents for photothermal therapy (PTT). The short blood circulation lifetime of AuNCs, however, limits their tumor uptake and thus *in vivo* applications. Here we show that such a limitation can be overcome by cloaking AuNCs with red blood cell (RBC) membranes, a natural stealth coating. The fusion of RBC membranes over AuNC surface does not alter the unique porous and hollow structures of AuNCs, and the resulting RBC-membrane-coated AuNCs (RBC-AuNCs) exhibit good colloidal stability. Upon NIR laser

irradiation, the RBC-AuNCs demonstrate *in vitro* photothermal effects and selectively ablate cancerous cells within the irradiation zone as do the pristine biopolymer-stealth-coated AuNCs. Moreover, the RBC-AuNCs exhibit significantly enhanced *in vivo* blood retention and circulation lifetime compared to the biopolymer-stealth-coated counterparts, as demonstrated using a mouse model. With integrated advantages of photothermal effects from AuNCs and long blood circulation lifetime from RBCs, the RBC-AuNCs demonstrate drastically enhanced tumor uptake when administered systematically, and mice that received PPT cancer treatment modulated by RBC-AuNCs achieve 100% survival over a span of 45 days. Taken together, our results indicate that the long circulating RBC-AuNCs may facilitate the *in vivo* applications of AuNCs, and the RBC-membrane stealth coating technique may pave the way to improved efficacy of PPT modulated by noble metal nanoparticles.
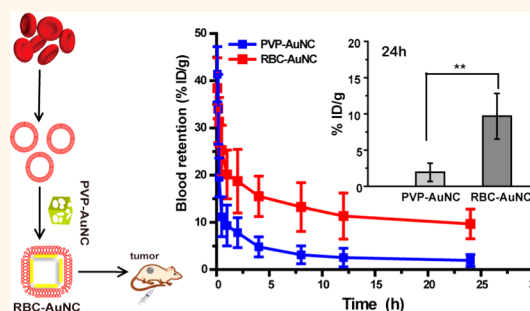
KEYWORDS: photothermal therapy · gold nanoparticle · membrane · tumor · blood circulation

P hotothermal therapy (PTT) utilizes photothermal conversion agents (PTCAs), which strongly absorb light and convert the absorbed light into heat, to generate rapid localized heating to preferentially ablate cancerous cells. Key factors dictating PTT efficacy include sufficient tissue penetration of the excitation light, large light-absorption cross section and high photothermal conversion efficiency of PTCAs, and their sustained systematic delivery to and consequently adequate accumulation within tumor *in vivo*.[1] To achieve deep tissue penetration as well as minimize heating of nontargeting tissues, near-infrared light (NIR, 650−900 nm) is generally the preferred excitation light, owing to its maximal

transmissivity in tissues and blood.[2,3] NIR PTCAs currently under active investigations include indocyanine green,[4,5] gold nanostructures (*e.g.*, nanoshell,[6,7] nanocage,[8−10] nanorod,[11−15] nanostar,[16] nanohexapod,[17] bellflower[18]), palladium nanoplates,[19] carbon nanotubes,[20−22] and graphene.[23−26] In particular, gold nanocages (AuNCs) have attracted significant research attention,[27,28] owing to their facile preparation,[29] tunable localized surface plasmon resonance (LSPR) band in the NIR region,[28,30] large NIR-absorption cross section,[31] high photothermal conversion efficiency per Au atom,[17,32] and the excellent biocompatibility of Au. As NIR PTCAs, AuNCs enable selective photothermal ablation of cancer cells both *in vitro*[8]

and *in vivo*.[9] Moreover, the unique hollow and porous structure of AuNCs confers them potentials as drug carriers; functionalized with temperature-responsive polymers, AuNCs have demonstrated controlled *in vitro* drug release *via* NIR photothermal effects,[33,34] indicative of potential applications in combinatorial chemo-photothermal therapy. However, even functionalized with polyethylene glycol (PEG), the current gold standard stealth molecule for nanoparticles, the resulting PEGylated AuNCs still demonstrated significantly rapid clearance from blood strain and limited tumor uptake *in vivo*. For example, at 24 h after injection, PEGylated AuNCs exhibit blood retention of <2% ID/g (percent of the injected dose per gram of tissue) and tumor uptake of only 2−8% ID/g.[17,35,36] Such short blood residence and limited tumor uptake largely limit the *in vivo* applications of AuNCs. It is thus imperative to develop techniques capable of extending the *in vivo* blood circulation lifetime of AuNCs.

Long-circulating nanoparticle therapeutics promises sustained systemic delivery and consequently enhanced accumulation within tumor *via* both passive and active targeting mechanisms.[37−39] To prolong the blood circulation lifetime and improve the colloidal stability *in vivo*, most nanoparticles developed for biomedical applications are coated with stealth materials.[1,38,39] PEG is the current gold standard molecule for providing stealth to nanoparticles because this molecule increases hydrophilicity, suppresses reticuloendothelial system (RES) uptake, and reduces nonspecific interactions between nanoparticles and blood components that may otherwise trigger immune attack.[40,41] Recent observations of anti-PEG immunological response have motivated the search for alternatives to PEG.[42] Membrane of red blood cells (RBCs, or erythrocytes) has recently been proposed as a superior alternative.[41,43] As nature's long circulating objects, RBCs have surface makeup comprising a myriad of "self-marker" proteins, glycans, and acidic sialyl moieties, which actively suppress the immune attack.[41,44,45] As stealth coating materials, RBC membranes completely cover the nanoparticle surface with their "self-markers" (*e.g.*, immunomodulatory proteins, glycans, and acidic sialyl moieties) mostly retained and in proper orientation (*i.e.*, right-side-out).[43,46,47] Inheriting RBCs' immune-suppressive surface makeup, RBC-membrane-coated polymeric nanoparticles have exhibited superior circulation half-life compared to their PEGlylated counterparts, as demonstrated using a mouse model.[43] This RBC-membrane-stealth coating technique has also significantly reduced the *in vitro* macrophage uptake of solid gold nanospheres.[48] Moreover, lipid-tethered targeting ligands spontaneously integrate into the natural RBC membranes, conferring the RBC-membrane-coated nanoparticles differential targeting to cancer cells *in vitro*,[49] indicative of a facile pathway toward both immune-suppression and active targeting.
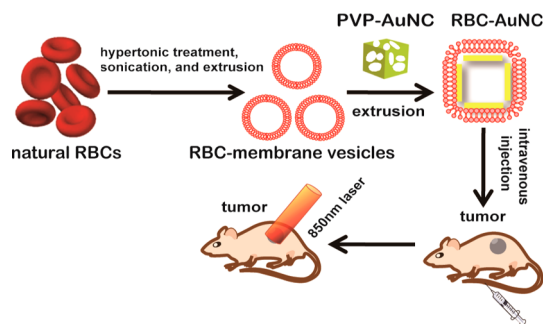

Figure 1. Schematic illustration of the preparation of RBC-membrane-coated gold nanocages (RBC-AuNCs), followed by PTT cancer treatment in mice.

In this work, we employ natural RBC membranes as stealth coating for AuNCs and aim for integrated advantages of long circulation lifetime from natural RBCs and photothermal effects from AuNCs. Our results demonstrate that, compared to the biopolymer-stealth-coated counterparts, our RBC-membrane-coated AuNCs exhibit superb *in vivo* blood circulation lifetime and blood retention and, in doing so, significantly enhanced tumor uptake and improved PTT efficacy in mice.

RESULTS AND DISCUSSION

The preparation of RBC-membrane-coated AuNCs (RBC-AuNCs) comprises three steps (Figure 1): preparing the pristine Au nanocages (AuNCs), deriving RBC membrane vesicles from natural RBCs, and fusing the RBC-membrane-derived vesicles over the surfaces of the pristine AuNCs. AuNCs were prepared *via* a galvanic replacement between Ag nanocubes and HAuCl$_4$.[29] The surfaces of the as-prepared AuNCs are intrinsically covered by poly(vinylpyrrolidone) (PVP, MW ∼ 50 000), a biopolymer potentially alternative to PEG.[42] Therefore, we call the as-prepared pristine Au nanocages PVP-AuNCs. RBC-derived-membrane vesicles were prepared *via* a procedure recently reported with slight modifications.[43,48] Briefly, the RBCs purified from the fresh blood of male imprinting control region (ICR) mice were washed with phosphate buffered saline (PBS) for three times and then subjected to a hypotonic treatment, to remove their intracellular contents. The resultant empty RBCs (*i.e.*, RBC ghosts) were subsequently washed with PBS and extruded sequentially through 400 nm and then 200 nm polycarbonate porous membranes, yielding RBC-membrane-derived vesicles with hydrodynamic diameters of ∼200 nm (Figure S1C, Supporting Information). We then fused the RBC-membrane-derived vesicles over the pristine PVP-AuNC surfaces by extruding their mixture through 200 nm polycarbonate porous membranes repeatedly, the mechanical force imposed by the extruding process facilitates the fusion of RBC membranes over nanoparticle surfaces,[43,48] leading to the expected RBC-AuNCs.

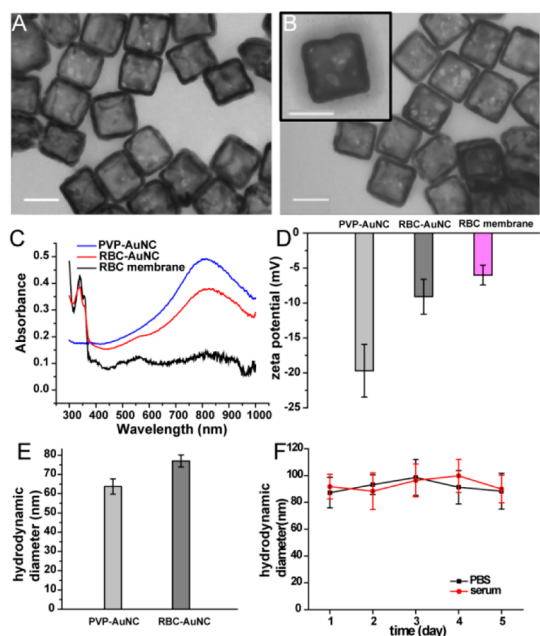The RBC-membrane coating on AuNCs was monitored by the changes in AuNC particle morphology,

Figure 2. (A,B) TEM images of AuNCs before (A) and after (B) the vesicle-AuNC fusion. Scale bar = 50 nm. (C−E) UV−vis−NIR absorption spectra (C), zeta potentials (D), and hydrodynamic diameters (E) of AuNCs before and after the vesicle-AuNC fusion; all samples were in PBS. (F) The hydrodynamic diameters of RBC-AuNCs in 1 × PBS and 100% fetal bovine serum (FBS) over a span of 5 days. Data points are reported as mean ± standard deviation.

optical absorption property, size, and surface charge before and after the vesicle-AuNC fusion process (Figure 2). TEM images show that the vesicle-AuNC fusion has not altered the unique hollow and porous structure of AuNCs. Closer examinations on the TEM images reveal that the vesicle-AuNC fusion has not impacted the characteristic dimensions of the AuNC cores (Figure S2). UV−vis−NIR spectra (Figure 2C) show that the vesicle-AuNC fusion step has barely altered the LSPR peak position of AuNCs (shifting slightly from ∼810 to ∼817 nm) but induced the appearance of an extra absorption peak at ∼350 nm, which agrees well with that of RBC membranes, indicative of successful transfer of RBC membranes onto the pristine PVP-AuNCs.[43,47] In addition, the vesicle-AuNC fusion has rendered the average zeta potential of nanoparticles decrease from −19.7 ± 3.78 to −9.1 ± 2.5 mV (Figure 2D and Figure S4), likely owing to the charge screening by RBC membranes as well as the less negative zeta-potential of RBC-membrane vesicles. This vesicle-AuNC fusion has also increased the average hydrodynamic diameter of nanoparticles from 71.20 nm (PDI = 0.282) to 89.05 nm (PDI = 0.288) (Figure 2E and Figure S5), and the extent of this increase (17.85 nm) corresponds well to the thickness of two layers of natural RBC membrane which is known to be 7.8 nm thick.[50] Taken together, these results indicate that RBC membranes together with their membrane proteins have been successfully fused onto the

exterior surfaces of PVP-AuNCs without significantly impacting the NIR optical property of AuNCs. Moreover, the resulting RBC-AuNCs exhibit good colloidal stability in both PBS and 100% fetal bovine serum (FBS), as indicated by the negligible increase in hydrodynamic diameter over a span of 5 days (Figure 2F).

One natural question that emerges is do the as-prepared RBC-AuNCs demonstrate integrated advantages of photothermal effects from AuNCs and long circulation lifetime of RBCs? To assess this, we first examine whether they retain the photothermal effects of AuNCs. Our *in vitro* photothermal conversion experiments indicate that the RBC-AuNCs exhibit similar NIR photothermal conversion effects as do the pristine PVP-AuNCs (Figure 3A). Upon irradiation with an 850 nm laser, both the RBC-AuNC dispersions and the PVP-AuNC dispersions (Au doses kept constant at 25 μg/mL) exhibit temperature rises, and higher irradiation power density generally leads to larger temperature rise with those ≥1 W/cm^2 leading to temperature rise of ≥15 °C within 2 min. In contrast, PBS without AuNCs exhibits <3 °C temperature rise even when having been irradiated at 2 W/cm^2 for 10 min. It is known that, at temperature above hyperthermia (42−47 °C),[51] cancerous cells could be selectively destroyed due to their reduced heat tolerance compared to normal cells.[52] Therefore, NIR irradiation power density of 1.0 W/cm^2 is used for all followed experiments unless specified otherwise, to achieve a temperature rise of ∼15 °C necessary for destroying cancerous cells within minutes.[53] Closer examinations on the kinetics of temperature rise reveal that, under comparable conditions, same irradiation power density and same irradiation time, both the rate and extent of temperature rise displayed by the RBC-AuNC dispersions are slightly lower than those by the PVP-AuNC dispersions (Figure 3A), likely due to the presence of RBC membranes on AuNC surfaces; an extra layer of stealth coating may hamper the heat dissipation into the surrounding solutions during photothermal conversion. Clearly, though less efficient than the pristine PVP-AuNCs, the RBC-AuNCs in aqueous solution still generate appreciable temperature rise *via* photothermal conversion effects.

To further characterize the RBC-AuNCs, we examine how NIR irradiations affect the stability of the RBC-membrane coating over the PVP-AuNCs and, as a result, the particles' photothermal conversion effects. As shown above, nonirradiated RBC-AuNCs exhibit negligible changes in hydrodynamic diameter over a span of 5 days (Figure 2F), indicating that the RBC-membrane coating should stay for at least 5 days in the absence of NIR irradiation. After 5 min NIR irradiation for just once, both the average zeta potential and the average hydrodynamic diameter of RBC-AuNCs shift from those of the nonirradiated RBC-AuNCs toward those of the pristine PVP-AuNCs (Figure S6), indicative
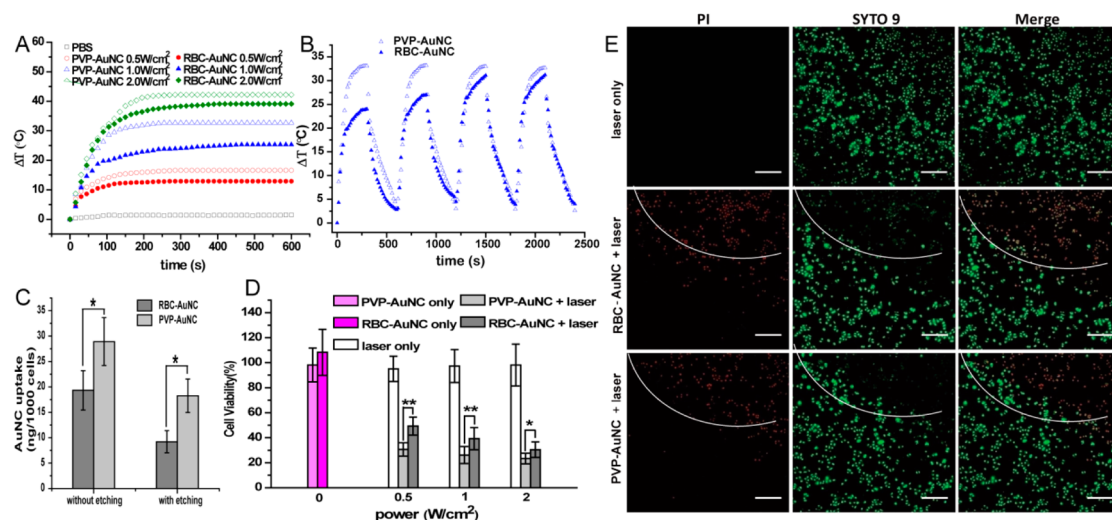
Figure 3. (A) Plots of temperature rise as a function of irradiation time for RBC-AuNC dispersions in PBS upon irradiation with an 850 nm laser at varying power densities. Similar experiments using PVP-AuNC dispersions in PBS are included for comparisons. Controls are PBS irradiated similarly with an 850 nm laser at 2.0 W/cm^2. (B) The relationship of temperature rise *versus* time for RBC-AuNC dispersion in PBS subjected to four cycles of NIR irradiation with an 850 nm laser at 1 W/cm^2 for 5 min and then cooling naturally to room temperature (*i.e.*, waiting for 5 min after turning off the laser). The performance of the pristine PVP-AuNCs assayed similarly is included as a reference. (C) Cell uptake studies reveal that the cell uptake of RBC-AuNCs is consistently lower than that of PVP-AuNCs, no matter whether the cell-surface-attached AuNCs are included (*i.e.*, without etching) or not (*i.e.*, with etching). Data points are reported as mean ± standard deviation. * indicates $p < 0.05$. (D) *In vitro* cell viability assays using RBC-AuNCs (Au content of 25 μg/mL) against HepG2 cells. Similar assays using PVP-AuNCs are included for comparisons. Clearly, upon NIR irradiation (850 nm laser for 10 min), both RBC-AuNCs and PVP-AuNCs result in significantly reduced cell viability. Controls that are assayed similarly but without laser irradiation indicate that neither RBC-AuNCs nor PVP-AuNCs are cytotoxic in the absence of NIR irradiation, and controls that are assayed similarly but without AuNC addition suggest that NIR irradiation is not cytotoxic either. Data points are reported as mean ± standard deviation. * and ** indicate $p < 0.05$ and $p < 0.01$, respectively. (C) Fluorescence confocal microscopy images show that, after 3-h treatment with RBC-AuNCs and NIR irradiation (with an 850 nm laser at 1 W/cm^2 for 10 min), cells inside the irradiation zone stain intensely red, indicative of dead cells, whereas those out of the irradiation zone remain dark in the red channel, indicative of live cells. Similar results are observed with the pristine PVP-AuNCs. In striking contrast, cells assayed similarly but without AuNC addition remain dark in the red channel, irrespective of their positions inside or out of the irradiation zone. Scale bar = 250 μm.

of partial ablation of the RBC-membrane coating from RBC-AuNCs. In contrast, even after 10 min NIR irradiation, the AuNC cores of RBC-AuNCs retain the original morphology and average characteristic dimensions according to their TEM images (Figure S7). Considering that the PVP-AuNCs in aqueous solutions generate faster and larger temperature rises than the RBC-AuNCs (Figure 3A), the partial loss of RBC-membrane coating may facilitate the heat dissipation during photothermal conversion and thus render the NIR-irradiated RBC-AuNCs generate faster and larger temperature rises. To examine whether this is the case, we subject the same RBC-AuNC dispersion to four irradiation-cooling cycles, with the performance of the pristine PVP-AuNCs as a reference; irradiation doses were kept constant with an 850 nm laser at 1.0 W/cm^2 for 5 min. Through the four irradiation-cooling cycles, the RBC-AuNCs consistently generate appreciable temperature rises upon NIR irradiation, likely owing to their unaffected AuNC cores (Figure S7), but the kinetics of temperature rise generated by them upon irradiation gradually shifts from that by the nonirradiated RBC-AuNCs toward that by the pristine PVP-AuNCs, which is barely impacted by the repeated irradiations (Figure 3B), likely owing to the partial loss of the

RBC-membrane coating (Figure S6). Taken together, these observations suggest that repeated NIR irradiations, usually involved in PTT cancer treatment *in vivo*, barely affect the AuNC cores of RBC-AuNCs but partially ablate their RBC-membrane coatings, rendering RBC-AuNCs more effective in generating appreciable temperature rises necessary for PTT cancer treatment.

To assess the *in vitro* cell uptake of RBC-AuNCs, we conduct the cell uptake studies using HepG2 cells as representative cancer cells. Briefly, we incubated ~10 000 HepG2 cells in Dulbecco's modified Eagle's medium (DMEM, 1 mL) with expected AuNCs (Au doses of 25 μg/mL) for 12 h at 37 °C, followed by PBS wash for three times. The cell uptake of AuNCs was determined by quantifying the Au content with an inductively coupled plasma mass spectrometry (ICP-MS). AuNCs internalized into cells are differentiated from those attached to cell surfaces *via* a procedure previously reported; after the 12-h incubation, samples were treated with an etchant based on I$_2$/KI which selectively dissolves Au nanostructures attached to cell surfaces without affecting those inside cells.[54,55] The results indicate that the cell uptake of RBC-AuNCs occurs *via* both cell internalization and cell-surface attachment, similar as that of PVP-AuNCs (Figure 3C).

Nevertheless, no matter whether or not the cell-surface-attached AuNCs are included, the cell uptake of RBC-AuNCs is consistently lower than that of PVP-AuNCs ($p < 0.05$) (Figure 3C), likely due to their increased particle size (Figure 2E).[54]

To evaluate whether the RBC-AuNCs ablate cancerous cells *via* NIR photothermal effects *in vitro*, we perform MTT assays using HepG2 cells as representative cancer cells. Briefly, $\sim$10 000 cells in DMEM were incubated with the RBC-AuNCs (Au dose of 25 μg/mL) for 3 h and subsequently irradiated with an 850 nm laser for 5 min. Upon NIR irradiation at power densities ranging 0.5–2.0 W/cm², cells treated with RBC-AuNCs consistently demonstrate significantly reduced viability as do those treated with the pristine PVP-AuNCs, and higher irradiation power density generally leads to lower cell viability (Figure 3D). For example, upon NIR irradiation at 0.5 W/cm², RBC-AuNCs and PVP-AuNCs lead to relative cell viability percentages of 49.34 and 30.65%, respectively, as compared to 30.5 and 23.4% upon NIR irradiation at 2.0 W/cm². In stark contrast, undetectable decrease in cell viability is observed for controls assayed similarly but without NIR irradiation as well as those assayed similarly but without AuNC addition. It should be noted that, upon irradiation at same NIR power density, RBC-AuNCs generally lead to appreciably reduced loss of cell viability *in vitro* compared to the pristine PVP-AuNCs (Figure 3D), likely due to their less efficient heat dissipation during photothermal conversion (Figure 3A) and impaired cell uptake (Figure 3C). Taken together, these results indicate that, similar as the PVP-AuNCs and the PEGylated AuNCs,[8] our RBC-AuNCs are intrinsically not cytotoxic but, upon NIR irradiation, effectively ablate cancerous cells *via* photothermal effects.

The ability of RBC-AuNCs to ablate cancerous cells *via* photothermal effects *in vitro* is further confirmed using fluorescence confocal microscopy (Figure 3E). Briefly, $\sim$50 000 HepG2 cells were incubated with AuNCs (Au content of 25 μg/mL) for 3 h, irradiate with an 850 nm laser at 1 W/cm² for 10 min, stained with SYTO 9 and propidium iodide (PI) in dark, and then examined under fluorescence confocal microscopy. SYTO 9 and PI are both nucleic acid stains but differ in both their spectra characteristics and capabilities to penetrate healthy cellular membranes. SYTO 9 is a cell-permeant green-fluorescent stain that labels both live and dead cells, whereas PI is a cell-impermeant red-fluorescent stain that only labels cells with compromised membranes. Upon NIR irradiation, AuNC-treated cells inside the irradiation zone stain intensely red, indicative of dead cells, whereas those out of the irradiation zone remain dark in the red channel, indicative of live cells; this is the case for both the RBC-AuNCs and the pristine PVP-AuNCs. In striking contrast, cells assayed similarly but without AuNC addition remain dark in the red channel, irrespective of

their positions inside or out of the irradiation zone. Taken together, the *in vitro* cell studies consistently demonstrate that the RBC-AuNCs successfully capture the advantage of effective photothermal conversion from AuNCs and ablate cancerous cells *via* photothermal effects *in vitro* with high efficiency.

Do the RBC-AuNCs also capture the advantage of long circulation lifetime from natural RBCs? To assess this, we conduct pharmacokinetics studies using a mouse model. Briefly, eight mice were used and randomly divided into two groups (n = 4 per group) and, into each mouse, 100 μL of 2.5 mg/mL expected AuNCs were injected through the tail vein. To avoid the immune response caused by blood cell type difference, we used the same mouse strain for pharmaceutics studies as that for collecting natural RBCs to prepare the RBC-AuNCs, as recommended previously.[41,43] At different time points after injection, 50 μL of blood were collected from mouse tail vein for followed Au content determination with ICP-MS. Our results show that the RBC-AuNCs consistently exhibit significantly enhanced blood retention over a span of 24 h, compared to the pristine PVP-AuNCs (Figure 4A). For example, at 12 and 24 h after injection, RBC-AuNCs exhibit blood retentions of 11.3% ID/g and 9.7% ID/g, respectively, as compared to only 2.5% ID/g and 1.9% ID/g by the PVP-AuNCs ($p < 0.01$) (Figure 4A and Figure S9). Note that, at 24 h after injection, even PEGylated AuNCs consistently demonstrate blood retentions of <2% ID/g.[17,35,36] Therefore, the RBC-AuNCs exhibit superior blood retention compared to their biopolymer-stealth-coated counterparts. Using a two-compartment model previously applied to fit the circulation results of nanoparticles,[43,56,57] we calculate the circulation half-life of the RBC-AuNCs to be 9.5 h, as compared to 1 h for the pristine PVP-AuNCs. The observed superior blood retention and circulation lifetime of RBC-AuNCs compared to those of PVP-AuNCs suggest that the immunosuppressive surface makeup of RBCs, which confer RBCs long circulation lifetime,[44,45] have been successfully translocated onto AuNC surfaces. Clearly, the RBC-AuNCs successfully achieve combined advantages of both the long circulation lifetime from natural RBCs and the photothermal effects from AuNCs.

Long *in vivo* circulation lifetime of nanoparticle therapeutics promises sustained systemic delivery and consequently enhanced accumulation within tumor *via* both passive and active targeting mechanisms.[37–39] Now that RBC-AuNCs exhibit superior blood retention and circulation lifetime compared to their biopolymer-stealth-coated counterparts, do they exhibit enhanced tumor uptake and improved biodistributions when administered systematically? To address this question, we perform biodistribution studies using a mouse model. Briefly, 16 mice bearing 4T1 tumor were randomly divided into two groups
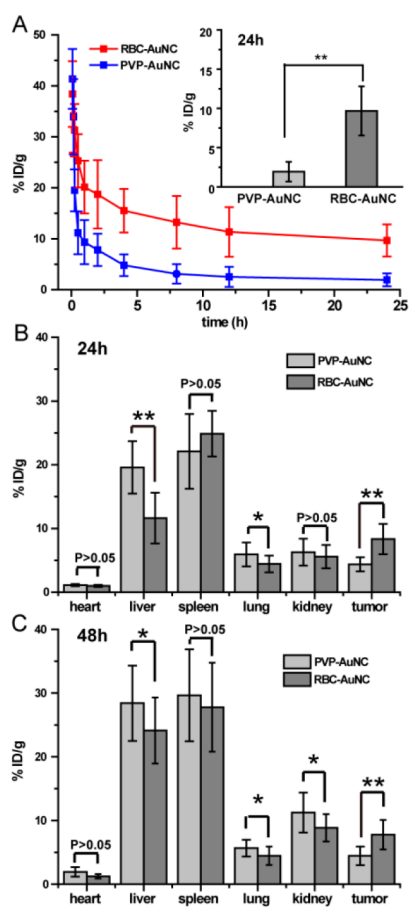
Figure 4. (A) Blood retentions of RBC-AuNCs and the pristine PVP- AuNCs over a span of 24 h. AuNCs were injected into mice through the tail vein, and at varying time points after AuNC injection, blood was withdrawn from mouse tail vein, and Au contents in blood were determined with ICP-MS. **(B,C)** Biodistributions of RBC-AuNCs and the pristine PVP- AuNCs at **(B)** 24 h and **(C)** 48 h after injection. AuNCs were injected intravenously into mice, and at 24 and 48 h after injection, organs and tumors of a randomly grouped subset of mice were collected, homogenized, and quantified for Au content with ICP-MS. Data points are reported as mean $\pm$ standard deviation. * and ** indicate $p < 0.05$ and $p < 0.01$, respectively.

($n = 8$ per group) and, into each mouse, 100 μL expected type of AuNCs (Au content of 2.5 mg/mL) were injected through the tail vein. At each time points (*i.e.*, 24 and 48 h) after injection, four mice from each group were sacrificed and their major organs (heart, liver, spleen, lung, and kidney) and tumors were collected for Au content determination with ICP-MS. At 24 and 48 h after injection, the RBC-AuNCs exhibit tumor uptakes of 8.34 $\pm$ 2.37 and 7.77 $\pm$ 2.31% ID/g, respectively, as compared to 4.37 $\pm$ 1.12 and 4.46 $\pm$ 1.46% ID/g by PVP-AuNCs (Figure 4B,C), indicative of significant enhancement in tumor uptake ($p < 0.01$). It should be noted that a seemingly small difference expressed in % ID/g may actually correspond to a huge difference expressed in number of particles accumulated within tumor. For example, at 48 h after injection, the difference in tumor uptake for RBC-AuNCs *versus*

PVP-AuNCs, approximately 3% ID/g, is estimated to correspond to a difference of approximately 10^{10} AuNC particles accumulated within tumor (please refer to Supporting Information for details). Note that our RBC-AuNCs are approximately 17 nm larger in hydrodynamic diameter than the pristine PVP-AuNCs (Figure 2E), and PEGylated AuNCs of larger size generally demonstrate lower tumor uptake.[17,35] Therefore, the relatively ~1.7−1.9-fold increase in tumor uptake for RBC-AuNCs *versus* PVP-AuNCs suggest that the facilitative effects imposed by the superior circulation lifetime and consequently enhanced permeation and retention (EPR) effects may have overwhelmed the impairing effects imposed by the increased particle size.[37−39,58] Decreasing the AuNC-core-size of RBC-AuNCs may further enhance their tumor uptake.

In addition to tumor, all the other five major organs examined exhibit certain AuNC accumulations at both examined time-points after injection and, in the order of decreasing extents, they are spleen, liver, kidney, lung, and heart for both the RBC-AuNCs and the PVP-AuNCs (Figure 4B,C). It is worth noting that, in addition to enhanced tumor uptake, the RBC-AuNCs also demonstrate significantly decreased accumulations within certain major organs compared to the PVP-AuNCs (Figure 4B,C). For example, at 24 h after injection, the accumulations of RBC-AuNCs within liver and lung are significantly lower than those of PVP-AuNCs ($p < 0.01$ and $p < 0.05$ for liver and lung, respectively) (Figure 4B). Similarly, at 48 h after injection, the accumulations of RBC-AuNCs within liver, lung, and kidney are significantly lower than those of PVP-AuNCs ($p < 0.05$) (Figure 4C). Taken together, these observations suggest that the RBC membrane coating confers the resulting RBC-AuNCs improved biodistributions.

Still, we have to notice that the biodistributions of RBC-AuNCs are far from being optimal. For example, the RBC-AuNCs demonstrate relatively highest accumulations within liver and spleen, two primary RES organs, as do the PVP-AuNCs (Figure 4B,C), despite their significantly differing blood retentions and circulation lifetimes (Figure 4A). Prior studies have reported that the PEGylated AuNCs also demonstrate relatively highest accumulations in liver and spleen.[9,17,35,36] Considering that these functionalized AuNCs, though having differing stealth coating materials, all have AuNCs as the core materials in common, their homogeneous prone accumulations in the RES system may be ascribed to the intrinsically rigid and cubic nature of their AuNC cores. To further improve the biodistributions of RBC-AuNCs, decreasing the AuNC-core size and functionalizing RBC-membrane-stealth with active targeting ligands may be pathways worth of future research efforts.

Clearly, the RBC-AuNCs have integrated both the photothermal conversion effects from the AuNC cores
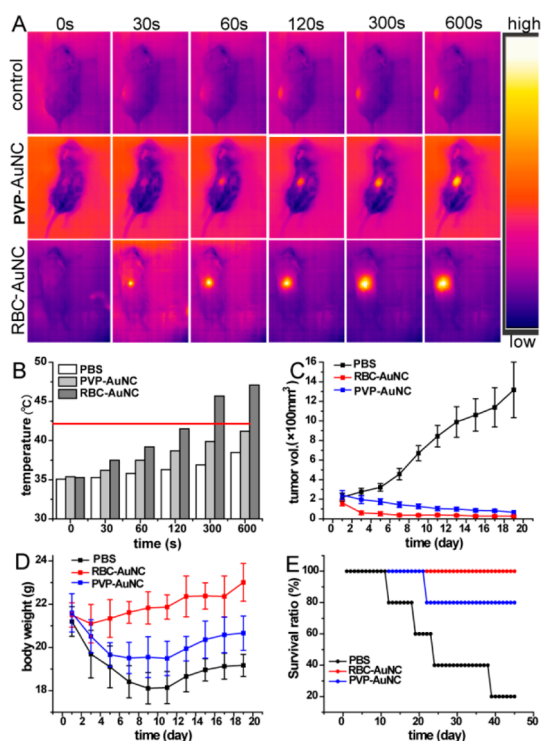
Figure 5. (A) Thermographs of mice injected with the RBC-AuNCs and the pristine PVP-AuNCs and, at 48 h after injection, irradiated with an 850 nm laser at power density of 1W/cm². Thermographs were recorded with an infrared thermal camera as a function of irradiation time. Mice assayed similarly but injected with PBS only are included as a reference. (B) Plots of temperature at tumor site as a function of irradiation time based on thermographs of mice in (A). Red line indicates 42 °C, the lowest boundary of hyperthermia temperature for selectively ablating cancerous cells in minutes. (C,E) Plots of the average tumor volume (C), average mouse body weight (D), and mouse survival ratio (E) of mice from different treatment groups as a function of time after initiation of NIR irradiation. The *in vivo* PTT cancer treatment was administered on mice injected with 100 μL RBC-AuNCs (Au content of 2.5 mg/mL) and, at 48 h after injection, irradiated with an 850 nm laser at 1 W/cm² for 10 min. Mice treated similarly but injected with PVP-AuNCs are included for comparisons. Controls are mice treated similarly but injected with PBS. Data points are reported as mean ± standard deviation.

and the long blood circulation lifetime from the RBC-membrane coating. When administered systematically for *in vivo* PTT cancer treatment, can the RBC-AuNCs out-perform the PVP-AuNCs? To assess this, we conduct *in vivo* PTT cancer treatments modulated by RBC-AuNCs using a mouse model, with the performance of the pristine PVP-AuNCs as a reference. Nine female Balb/c mice bearing 4T1 tumors were used and randomly divided into three groups ($n = 3$ per group). Each mouse was injected through the tail vein with expected type of AuNCs at same Au dose of 250 μg and, at 48 h after injection, irradiated with an 850 nm laser at power density of 1 W/cm² and photographed using an infrared thermal camera (Figure 5A). At 10 min after initiation of NIR irradiation, the temperature at tumor site of mouse treated with RBC-AuNCs increases

to 47.1 °C, as compared to 41.2 °C for mouse treated with the pristine PVP-AuNCs (Figure 5B), likely owing to the significantly enhanced tumor uptake of RBC-AuNCs (Figure 4C and Supporting Information).

It is known that, at temperatures above hyperthermia (42−47 °C),[51] tumor will be selectively destroyed due to their reduced heat tolerance compared to normal cells.[52] Therefore, the RBC-AuNCs may lead to improved efficacy in PTT cancer treatment *in vivo* compared to the pristine PVP-AuNCs. This is indeed the case. Efficacy of *in vivo* PTT cancer treatment is gauged by monitoring the average tumor volume, the average mouse body weight, and the mouse survival over a span of 19 days starting from 48 h after injection (Figure 5C−E). Briefly, 15 mice bearing 4T1 tumor were used and randomly divided into three groups ($n = 5$ per group) and, among them, two groups were injected with 100 μL either RBC-AuNCs or PVP-AuNCs in PBS (Au content of 250 μg) whereas the other group were injected with 100 μL PBS. At 48 h after injection, each mouse was irradiated with an 850 nm laser at 1 W/cm² for 10 min. Through the following 19 days, both AuNC-injected groups demonstrate consistently decreasing average tumor volumes irrespective of the presence or absence of RBC-membrane coating, whereas the PBS-injected control group demonstrate consistently increasing average tumor volume (Figure 5C), indicative of PTT efficacy conferred by the AuNC cores. Moreover, the average tumor volume of mice injected with RBC-AuNCs decreases at faster rate and reaches a smaller final value than that of mice injected with PVP-AuNCs, indicative of improved PTT efficacy conferred by the RBC-membrane-stealth coating. Similar results are observed when gauging the PTT efficacy *in vivo* with average mouse body weights (Figure 5D). Over a span of 19 days, mice injected with RBC-AuNCs exhibit consistently increasing average body weight, indicative of appreciable PTT efficacy and unnoticeable toxic side-effects. In contrast, mice injected with PVP-AuNCs exhibit quick drop in average body weight during the first 5 days after initiation of NIR irradiation and fail in recovering the initial average body weight even at the end of the experiment (*i.e.*, the 19th day), as do those injected with PBS (Figure 5D), indicative of worse PTT efficacy than that by RBC-AuNCs. We further gauge the PTT efficacy *in vivo* with mouse survival over a span of 45 days starting from 48 h after injection. Our results reveal that, through these 45 days, all the five mice injected with RBC-AuNCs remain alive, indicative of 100% survival, whereas those injected with PVP-AuNCs or PBS exhibit loss of survival to varying extent (Figure 5E). One of the five mice injected with PVP-AuNCs died on the 19th day after initiation of NIR irradiation, indicative of 80% survival, and four of the five mice injected with PBS died during the PTT treatment time range, indicative of only 20% survival. Note that the RBC-AuNCs contain similar amount of
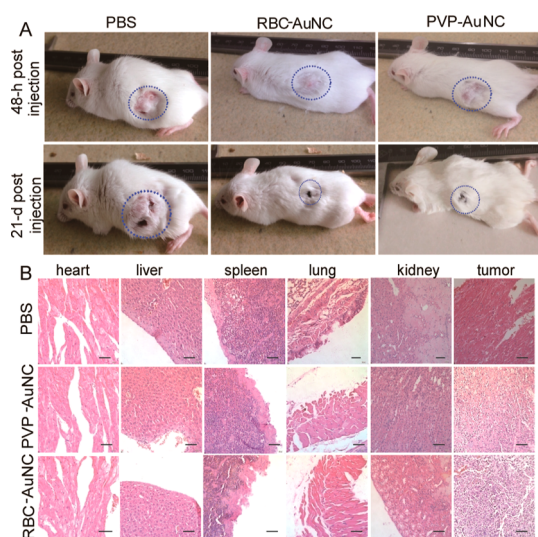
Figure 6. (A) Photographs of mice at 48 h after injection (*i.e.*, prior to initiation of NIR irradiation) and on the 19th day after initiation of NIR irradiation (*i.e.*, 21st day after injection). (B) Hematoxylin and eosin (H&E) stained sections of major organs and tumors collected from different treatment groups of mice on the 19th day after initiation of NIR irradiation, when tumors of mice in the RBC-AuNC-treatment group shrunk to negligible sizes. Scale bar = 50 μm.

PVP molecules as do the pristine PVP-AuNCs. Taken together, the above three independent indices, average tumor volume, mouse body weight, and mouse survival, consistently demonstrate that the RBC-AuNCs out-perform the PVP-AuNCs when administered systematically for *in vivo* PTT cancer treatment. Considering that the RBC-AuNCs demonstrate lower *in vitro* PTT efficacy in cell studies than the PVP-AuNCs (Figure 3), the as-observed improvement in efficacy of *in vivo* PTT cancer treatment must originate in the superior blood circulation lifetime and tumor uptake conferred by the RBC-membrane-stealth coating.

Nanotoxicity is always a major concern for the *in vivo* applications of nanotherapeutics. High toxicity usually leads to drop in body weight. As shown in Figure 5D, treatment of RBC-AuNCs lead to consistent increase, rather than drop, in average mouse body weight over a span of 19 days, indicative of lack of high toxicity. To examine whether the RBC-AuNC-treatment causes damages to the major organs, we perform histology analysis *via* standard histological techniques with hematoxylin and eosin (H&E) staining. On the 21st day after injection, when mice treated with RBC-AuNCs have their tumors shrunk to negligible sizes by PTT

(Figure 6A), major organs and tumors of treated mice were collected for subsequent histology analysis. Slices of major organs (heart, liver, spleen, lung, and kidney) of mice treated with RBC-AuNCs or PVP-AuNCs exhibit no noticeable abnormality or lesion compared to those of the controls, mice treated with PBS (Figure 6B), indicative of lack of appreciable organ damages and thus suggesting promise of using RBC-AuNCs for *in vivo* applications. In contrast to the organ slices, the tumor slices differ drastically depending on whether or not mice are treated with AuNCs (Figure 6B). Tumor slices of mice treated with RBC-AuNC or PVP-AuNCs exhibit apparent abnormality or lesion compared to those of the PBS-treated mice (Figure 6B), indicative of efficient ablation of cancer cells, consistent with their observed inhibition on cancer growth (Figure 5C). Moreover, more obvious abnormality or lesion are observed in tumor slices of the RBC-AuNC-treated mice than in those of the PVP-AuNC-treated ones (Figure 6B), consistent with their improved PTT efficacy *in vivo* (Figure 5C–E). Taken together, these observations suggest that the treatment of RBC-AuNCs at Au dose of 250 μg within 21 days, though effective in eliminating tumor *via* PTT, poses no obvious signals of toxic side-effects in mice.

CONCLUSIONS

In summary, we have successfully fused natural RBC membranes onto surfaces of the pristine PVP-AuNCs, resulting in the RBC-AuNCs that perfectly integrate the effective photothermal conversion effects of AuNC cores with the long circulation lifetime of natural RBCs. Using a mouse model, we have demonstrated that the as-prepared RBC-AuNCs exhibit superior blood retention and circulation lifetime to their biopolymer-stealth-coated counterparts. As a result, the RBC-AuNCs, when administered systematically for *in vivo* PTT cancer treatment, demonstrate significantly enhanced tumor uptake and improved efficacy without causing noticeable damages to major organs. To further improve the biodistributions and tumor uptake of RBC-AuNCs, potential pathways worth of future efforts include decreasing the nanocage size and functionalizing the RBC membranes with active targeting ligands. This work suggests that the RBC-AuNCs may facilitate the *in vivo* applications of AuNCs, and the RBC-membrane-stealth coating technique may open possibilities of improving efficacy for *in vivo* PPT cancer treatment modulated by noble metal nanoparticles *via* surface engineering.

MATERIALS AND METHODS

Preparation of Gold Nanocages. Gold nanocages (AuNCs) were prepared using a galvanic replacement between silver nanocubes and chlorauric acid (HAuCl$_4$) previously reported.[29] Briefly, Ag nanocubes were first synthesized: 10 mL of ethylene glycol (Sigma-Aldrich) was heated under magnetic stirring in oil

bath to 150 °C. 0.12 mL of NaSH solution (3 mM in EG, Sigma-Aldrich) was quickly added into the heated solution. Four minutes later, 1 mL of HCl solution was quickly added. The HCl solution was prepared by adding 4 μL of HCl into 12 mL of EG. After 2 min, 2.5 mL poly(vinylpyrrolidone) solution (PVP, 20 mg·mL^{-1} in EG, MW $\approx$ 55 000, Sigma-Aldrich) was added. After another 2 min, 0.8 mL of CF$_3$COOAg solution (282 mM in

EG, Aldrich) was added into the mixture. The mixture was maintained at 150 °C for 1 h. The samples were washed with acetone once and water twice and stored in water for further use. For Au nanocages, adequate amount of as-stored Ag nanocubes were added into 20 mL of H_2O. Once the mixture was heated to 90 °C, 0.6-mM $HAuCl_4$ aqueous solution was injected at a rate of 0.2 mL/min. UV–vis absorption spectra were used to monitor the progress. The injection was stopped until the appropriate SPR peak was obtained. The mixture was stirred for another 10 min. Then samples were purified and washed and finally dispersed in deionized (DI) water.

Preparation of RBC-Membrane-Derived Vesides. The RBC-membrane-derived vesicles were prepared using a procedure previously reported,[43] which consists primary two steps: deriving RBC ghosts from natural RBCs, and preparing RBC-membrane-derived vesicles from RBC ghosts.

RBC ghosts were prepared by subjecting natural RBCs to hypertonic treatment. Briefly, fresh whole blood withdrawn from male imprinting control region (ICR) mice (6–8 wk) obtained from the Animal Center at Anhui Medical University was centrifuged at 800 rcf for 5 min at 4 °C and the resultant packed RBCs were washed with ice cold 1× PBS for three times, to remove the plasma and the buffy coat. The as-washed RBCs were then subjected to a hypotonic treatment, to remove their intracellular contents; briefly, washed RBCs were resuspended into 1/4× PBS, kept in an ice bath for 20 min, and subsequently centrifuged at 800 rcf for 5 min. The supernatant which contains the released hemoglobin was discarded, and the light-pink pellet which contains the RBC ghosts was collected and washed with 1× PBS twice. The preparation of RBC ghosts was monitored using a Live Cell Workstation (AF6000LX, Leica), which revealed an intact cellular shape but an altered intracellular content (Figure S1A,B).

The RBC-membrane-derived vesicles were prepared from the as-obtained RBC-ghosts. Briefly, RBC ghosts were sonicated in a capped glass vial for 5 min using a bath sonicator at a frequency of 53 kHz and a power of 100 W, and subsequently extruded sequentially through 400 nm and then 200 nm polycarbonate porous membranes with an Avanti mini extruder (Avanti Polar Lipids). The preparation of RBC-membrane-derived vesicles was monitored by measuring the hydrodynamic diameters and zeta-potentials of products after each step (Figure S1C,D), using a nanoparticle analyzer (Nano-ZS90, Malvern).

Fusion of RBC Membranes onto the Surfaces of PVP-AuNC Particles. 1 mL of AuNCs at Au content of 25 μg/mL was mixed with RBC-membrane-derived vesicles derived from 1 mL of whole blood; both were in PBS. The resultant mixture was subsequently extruded for 7 times through a 200 nm polycarbonate porous membrane using an Avanti mini extruder, followed by centrifugation at 3500 rcf to remove excess RBC-membrane-derived vesicles, yielding the RBC-membrane-fused AuNCs (RBC-AuNCs).

Characterizations of AuNCs before and after RBC Membrane Fusion. The morphologies of AuNCs were characterized using a transmission electron microscope (TEM) (H-7650, Hitachi) operating at 100 kV; prior to TEM characterizations, one drop of an AuNC suspension was added onto a carbon-coated copper grid and dried under ambient conditions, followed by TEM imaging. The hydrodynamic diameters and zeta potentials of AuNCs in PBS (Au concentration of 25 μg/mL) were measured using nanoparticle analyzer (Nano-ZS90, Malvern) at 25 °C. UV–vis–NIR absorption spectra of AuNCs in PBS (Au content of 25 μg/mL) were recorded using a UV–vis spectrometer (Cary 60 UV–vis, Agilent).

In Vitro Photothermal Conversion Characterizations. The in vitro photothermal conversion effects of AuNCs were characterized by monitoring the temperature rise of AuNC dispersions (500 μL) in phosphate buffered saline (PBS) upon irradiation of an 850 nm laser at varying power densities as a function of irradiation time; both RBC-AuNCs and the pristine PVP-AuNCs were at Au content of 25 μg/mL, which is estimated to correspond to an AuNC number density of approximately 10^{10} particles/mL, the minimal threshold number density for PEGylated AuNC dispersions to achieve temperature rise of 15 °C[9] necessary for destroying cancerous cells within minutes.[53]

To assess how repeated NIR irradiations affect the photothermal conversion effects of RBC-AuNCs, we subjected the same RBC-AuNC dispersion to four irradiation-cooling cycles. Briefly, 500 μL RBC-AuNC dispersion in PBS (Au content at 25 μg/mL) was irradiated with an 850 nm laser at 1 W/cm^2 for 5 min, and then cooled naturally to room temperature (i.e., waiting for 5 min after ceasing the irradiation); this irradiation-cooling cycle was repeated for four times.

In Vitro Cell Uptake Studies. Approximately 100 000 cells in Dulbecco's modified Eagle's medium (DMEM, SH30022.01B, Hyclone) supplemented with 10% FBS were seeded into a well of a 12-well plate, incubated at 37 °C for 24 h until reaching ~80% confluence, washed with PBS twice, incubated in FBS-absent DMEM with RBC-AuNCs (Au dose of 25 μg/mL) for 12 h, and washed with PBS for three times. To differentiate AuNCs internalized into cells from those attached to cell surfaces, we carried out an etching procedure as previously reported.[54,55] Briefly, after the 12-h incubation, samples were treated with a solution (1 mL) composed of I_2 (0.34 mM) and KI (2.04 mM) for 5 min, followed by PBS wash for three times; this I_2/KI solution selectively dissolves Au nanostructures attached to cell surfaces without affecting those inside cells.[54,55]

Subsequently, samples were treated with trypsin, for cell-number quantification, and then aqua regia to dissolve Au. The resulting solutions were left standing still at room temperature for 6 h and then heated at the temperature of 60 °C for 12 h to remove aqua regia. The residuals were dissolved in DI water, for followed Au content determination using an inductively coupled plasma mass spectrometry (ICP-MS). Comparable measurements on solutions with known Au concentrations were performed, which yielded the calibration curve (Figure S8). Each trial was carried out in triplicate, and the reported results are averages of two independent trials.

In Vitro PTT Cell Studies. HepG2 cells were used as representative cancerous cells. The in vitro cytotoxicity of the as-prepared RBC-AuNCs was assessed with MTT assays, using 3-[4,5-dimethylthiazol-2-yl]-2,5-diphenyltetrazolium bromide (MTT, 98%, Sigma-Aldrich). Briefly, approximately 10 000 cells in Dulbecco's modified Eagle's medium (DMEM, SH30022.01B, Hyclone) supplemented with 10% FBS were seeded into a well of a 96-well plates, incubated at 37 °C for 24 h until reaching ~80% confluence, washed with PBS twice, incubated in FBS-absent DMEM with RBC-AuNCs at varying concentrations for 3 h, and subsequently irradiated with an 850 nm laser at 1 W/cm^2 for 5 min. Relative cell viabilities were determined by monitoring the optical densities at 490 and 570 nm with a microplate reader (Varioskan, Thermo). Comparable assays using the pristine PVP-AuNCs are included for parallel comparisons. Controls include those assayed similarly but without AuNC addition to indicate 100% cell viability as well as those assayed similarly but without laser irradiation to indicate the intrinsic cytotoxicity of AuNCs. Each trial was carried out in triplicate and the reported results are averages of two independent trials.

Whether RBC-AuNCs were capable of ablating cancerous cells via photothermal effects in vitro was also evaluated using laser scanning fluorescence confocal microscopy. Briefly, approximately 50 000 HepG2 cells were seeded into a culture dish specifically designed for use with a confocal microscopy, incubated at 37 °C under 5% CO^2 conditions for 24 h until reaching ~80% confluency, treated with RBC-AuNCs (Au dose of 25 μg/mL) for 3 h, and subsequently irradiated with a 850 nm laser at 1 W/cm^2 for 5 min. The irradiated cells were then stained with SYTO 9 and propidium iodide (PI) (Molecular Probes) in dark for 30 min, washed with 1× PBS once, and imaged under a fluorescence confocal microscope (SP5, Leica). Laser lines of 485 and 535 nm at approximately 20% of their maximum intensity were used to excite SYTO 9 and PI, respectively. Comparable assays using the pristine PVP-AuNCs are included for parallel comparisons. Controls are those assayed similarly but without AuNC addition.

Pharmacokinetics Studies. Eight male ICR mice (6–8 wk) obtained from the Animal Center of Anhui Medical University were used and randomly divided into two groups (n = 4 per group) and, into each mouse, 100 μL of expected type of AuNCs in PBS (Au content of 2.5 mg/mL) were injected through the tail vein.

At varying time-points after injection (*i.e.*, 1, 5, 15, 30 min, and 1, 2, 4, 8, 24 h), 50 μL blood were collected from mouse tail vein for the followed Au content determination with an inductively coupled plasma mass spectrometry (ICP-MS). All animal experiments were conducted in compliance with the guidelines for the care and use of research animals established by the Animal Care and Use Committee at University of Science and Technology of China.

Samples for ICP-MS measurements were prepared as follows. 50 μL of freshly withdrawn blood was added into 1 mL of aqua regia, and the resultant mixture was left standing-still at room temperature for 12 h and then kept in oil bath at 80 °C for 6 h to remove acids. The residual was subsequently resuspended into 1 mL of deionized (DI) water and filtered through a 0.22 μm membrane filter unit (Millipore), yielding samples for Au content quantification with ICP-MS (Optima 7000 DV, PerkinElmer). Comparable measurements on solutions with known Au concentrations were performed, which yielded the calibration curve (Figure S8).

Biodistribution Studies. BALB/c mouse bearing 4T1 murine breast tumor was used as mouse model for biodistribution studies. BALB/c mice (3−4 wk) were obtained from the Animal Center at Anhui Medical University and, into the left rear flank of each mouse, $\sim 3 \times 10^5$ 4T1 murine breast cancer cells in 100 μL PBS was subcutaneously injected, yielding the 4T1 tumor model. Sixteen mice bearing 4T1 tumor were used and divided into two groups ($n = 8$ per group) and, into each mouse, 100 μL expected type of AuNCs (Au content of 2.5 mg/mL) was injected through the tail vein. At 24 and 48 h after injection, four mice from each group were randomly selected and sacrificed, and their livers, kidneys, spleens, lungs, hearts, and tumors were collected and completely digested with 4 mL of aqua regia for Au content determination with ICP-MS. The Au content in each organ was expressed as percent of the injected Au dose per gram of tissue (% ID/g).

***In Vivo* PTT Cancer Treatment.** Fifteen BALB/c mice bearing 4T1 tumor were used and randomly divided into three groups ($n = 5$ per group) and, among them, two groups were injected with 100 μL expected type of AuNCs (Au content of 2.5 mg/mL), whereas the other group were injected with 100 μL PBS; all injections were administered intravenously through the tail vein. At 48 h after injection, all mice were anesthetized with 3% neodorm, and their tumors were irradiated with an 850 nm laser at a power density of 1.0 W/cm^2 for 10 min; the NIR laser was coupled to a 100 mm-core fiber with the spot size of the laser beam adjusted to cover the entire tumor regions. During irradiation, thermographs of mice were recorded with an infrared thermal camera (ICI7320, Infrared Camera Inc.), and on the basis of the as-obtained thermographs, temperatures at tumor sites were obtained. The NIR irradiation was repeated once a day ever since over a span of 19 days, during which tumor lengths and widths were measured with a caliper and mouse body weights were measured using a scale-balance every other day. Tumor volume was calculated as the volume V = (tumor length) × (tumor width)^2/2.

Histology Analysis. On the 21st day after injection (*i.e.*, the 19th day after initiation of NIR irradiation), one mouse from each group was randomly selected and sacrificed for histology analysis; the mouse which received PTT cancer treatment modulated by PVP-AuNCs but died on the 19th day after initiation of NIR irradiation was used. Organs including liver, spleen, kidney, heart, lung, and tumor of these mice were collected, fixed in 10% neutral buffered formalin, processed routinely into paraffin, sectioned at 8 μm, stained with hematoxylin and eosin (H&E), and examined using an inverted fluorescence microscope (IX81, Olympus).

Statistical Analysis. Statistical comparisons were carried out by performing student *t* test analysis with the statistical software package BioMedCalc (version 2.9). *p* values of <0.05 and <0.01 indicate statistical difference and statistically significant difference, respectively.

REFERENCES AND NOTES

1. Kennedy, L. C.; Bickford, L. R.; Lewinski, N. A.; Coughlin, A. J.; Hu, Y.; Day, E. S.; West, J. L.; Drezek, R. A. A New Era for Cancer Treatment: Gold-Nanoparticle-Mediated Thermal Therapies. *Small* **2011**, *7*, 169–183.
2. Weissleder, R. A Clearer Vision for *In Vivo* Imaging. *Nat. Biotechnol.* **2001**, *19*, 316–317.
3. Weissleder, R.; Ntziachristos, V. Shedding Light onto Live Molecular Targets. *Nat. Med.* **2003**, *9*, 123–128.
4. Zheng, M.; Yue, C.; Ma, Y.; Gong, P.; Zhao, P.; Zheng, C.; Sheng, Z.; Zhang, P.; Wang, Z.; Cai, L. Single-Step Assembly of DOX/ICG Loaded Lipid−Polymer Nanoparticles for Highly Effective Chemo-Photothermal Combination Therapy. *ACS Nano* **2013**, *7*, 2056–2067.
5. Zheng, X.; Zhou, F.; Wu, B.; Chen, W. R.; Xing, D. Enhanced Tumor Treatment Using Biofunctional Indocyanine Green-Containing Nanostructure by Intratumoral or Intravenous Injection. *Mol. Pharmaceutics* **2012**, *9*, 514–522.
6. Hirsch, L. R.; Stafford, R. J.; Bankson, J. A.; Sershen, S. R.; Rivera, B.; Price, R. E.; Hazle, J. D.; Halas, N. J.; West, J. L. Nanoshell-Mediated Near-Infrared Thermal Therapy of Tumors under Magnetic Resonance Guidance. *Proc. Natl. Acad. Sci. U. S. A.* **2003**, *100*, 13549–13554.
7. Carpin, L.; Bickford, L.; Agollah, G.; Yu, T.-K.; Schiff, R.; Li, Y.; Drezek, R. Immunoconjugated Gold Nanoshell-Mediated Photothermal Ablation of Trastuzumab-Resistant Breast Cancer Cells. *Breast Cancer Res. Treat.* **2011**, *125*, 27–34.
8. Chen, J.; Wang, D.; Xi, J.; Au, L.; Siekkinen, A.; Warsen, A.; Li, Z.-Y.; Zhang, H.; Xia, Y.; Li, X. Immuno Gold Nanocages with Tailored Optical Properties for Targeted Photothermal Destruction of Cancer Cells. *Nano Lett.* **2007**, *7*, 1318–1322.
9. Chen, J.; Glaus, C.; Laforest, R.; Zhang, Q.; Yang, M.; Gidding, M.; Welch, M. J.; Xia, Y. Gold Nanocages as Photothermal Transducers for Cancer Treatment. *Small* **2010**, *6*, 811–817.
10. Gao, L.; Fei, J.; Zhao, J.; Li, H.; Cui, Y.; Li, J. Hypocrellin-Loaded Gold Nanocages with High Two-Photon Efficiency for Photothermal/Photodynamic Cancer Therapy *In Vitro*. *ACS Nano* **2012**, *6*, 8030–8040.
11. Huang, X.; El-Sayed, I. H.; Qian, W.; El-Sayed, M. A. Cancer Cell Imaging and Photothermal Therapy in the Near-Infrared Region by Using Gold Nanorods. *J. Am. Chem. Soc.* **2006**, *128*, 2115–2120.
12. Huang, X.; Jain, P.; El-Sayed, I.; El-Sayed, M. Plasmonic Photothermal Therapy (PPTT) Using Gold Nanoparticles. *Laser Med. Sci.* **2008**, *23*, 217–228.
13. Tsai, M.-F.; Chang, S.-H. G.; Cheng, F.-Y.; Shanmugam, V.; Cheng, Y.-S.; Su, C.-H.; Yeh, C.-S. Au Nanorod Design as Light-Absorber in the First and Second Biological Near-Infrared Windows for *In Vivo* Photothermal Therapy. *ACS Nano* **2013**, *7*, 5330–5342.
14. Dickerson, E. B.; Dreaden, E. C.; Huang, X.; El-Sayed, I. H.; Chu, H.; Pushpanketh, S.; McDonald, J. F.; El-Sayed, M. A. Gold Nanorod Assisted Near-Infrared Plasmonic Photothermal Therapy (PPTT) of Squamous Cell Carcinoma in Mice. *Cancer Lett.* **2008**, *269*, 57–66.
15. Park, J.-H.; von Maltzahn, G.; Xu, M. J.; Fogal, V.; Kotamraju, V. R.; Ruoslahti, E.; Bhatia, S. N.; Sailor, M. J. Cooperative Nanomaterial System to Sensitize, Target, and Treat Tumors. *Proc. Natl. Acad. Sci. U. S. A.* **2010**, *107*, 981–986.
16. Yuan, H.; Fales, A. M.; Vo-Dinh, T. TAT Peptide-Functionalized Gold Nanostars: Enhanced Intracellular Delivery and Efficient NIR Photothermal Therapy Using Ultralow Irradiance. *J. Am. Chem. Soc.* **2012**, *134*, 11358–11361.

17. Wang, Y.; Black, K. C. L.; Luehmann, H.; Li, W.; Zhang, Y.; Cai, X.; Wan, D.; Liu, S.-Y.; Li, M.; Kim, P.; *et al.* Comparison Study of Gold Nanohexapods, Nanorods, and Nanocages for Photothermal Cancer Treatment. *ACS Nano* **2013**, *7*, 2068–2077.

18. Huang, P.; Rong, P.; Lin, J.; Li, W.; Yan, X.; Zhang, M. G.; Nie, L.; Niu, G.; Lu, J.; Wang, W.; *et al.* Triphase Interface Synthesis of Plasmonic Gold Bellflowers as Near-Infrared Light Mediated Acoustic and Thermal Theranostics. *J. Am. Chem. Soc.* **2014**, *136*, 8307–8313.

19. Huang, X.; Tang, S.; Mu, X.; Dai, Y.; Chen, G.; Zhou, Z.; Ruan, F.; Yang, Z.; Zheng, N. Freestanding Palladium Nanosheets with Plasmonic and Catalytic Properties. *Nat. Nanotechnol.* **2011**, *6*, 28–32.

20. Kam, N. W. S.; O'Connell, M.; Wisdom, J. A.; Dai, H. Carbon Nanotubes as Multifunctional Biological Transporters and Near-Infrared Agents for Selective Cancer Cell Destruction. *Proc. Natl. Acad. Sci. U. S. A.* **2005**, *102*, 11600–11605.

21. Moon, H. K.; Lee, S. H.; Choi, H. C. *In Vivo* Near-Infrared Mediated Tumor Destruction by Photothermal Effect of Carbon Nanotubes. *ACS Nano* **2009**, *3*, 3707–3713.

22. Robinson, J. T.; Welsher, K.; Tabakman, S. M.; Sherlock, S. P.; Wang, H. L.; Luong, R.; Dai, H. J. High Performance *In Vivo* Near-IR (> 1 μm) Imaging and Photothermal Cancer Therapy with Carbon Nanotubes. *Nano Res.* **2010**, *3*, 779–793.

23. Yang, K.; Zhang, S.; Zhang, G.; Sun, X.; Lee, S.-T.; Liu, Z. Graphene in Mice: Ultrahigh *In Vivo* Tumor Uptake and Efficient Photothermal Therapy. *Nano Lett.* **2010**, *10*, 3318–3323.

24. Robinson, J. T.; Tabakman, S. M.; Liang, Y.; Wang, H.; Sanchez Casalongue, H.; Vinh, D.; Dai, H. Ultrasmall Reduced Graphene Oxide with High Near-Infrared Absorbance for Photothermal Therapy. *J. Am. Chem. Soc.* **2011**, *133*, 6825–6831.

25. Li, M.; Yang, X.; Ren, J.; Qu, K.; Qu, X. Using Graphene Oxide High Near-Infrared Absorbance for Photothermal Treatment of Alzheimer's Disease. *Adv. Mater.* **2012**, *24*, 1722–1728.

26. Markovic, Z. M.; Harhaji-Trajkovic, L. M.; Todorovic-Markovic, B. M.; Kepic, D. P.; Arsikin, K. M.; Jovanovic, S. P.; Pantovic, A. C.; Dramicanin, M. D.; Trajkovic, V. S. *In Vitro* Comparison of the Photothermal Anticancer Activity of Graphene Nanoparticles and Carbon Nanotubes. *Biomaterials* **2011**, *32*, 1121–1129.

27. Chen, J.; Yang, M.; Zhang, Q.; Cho, E. C.; Cobley, C. M.; Kim, C.; Glaus, C.; Wang, L. V.; Welch, M. J.; Xia, Y. Gold Nanocages: A Novel Class of Multifunctional Nanomaterials for Theranostic Applications. *Adv. Funct. Mater.* **2010**, *20*, 3684–3694.

28. Xia, Y.; Li, W.; Cobley, C. M.; Chen, J.; Xia, X.; Zhang, Q.; Yang, M.; Cho, E. C.; Brown, P. K. Gold Nanocages: From Synthesis to Theranostic Applications. *Acc. Chem. Res.* **2011**, *44*, 914–924.

29. Skrabalak, S. E.; Au, L.; Li, X.; Xia, Y. Facile Synthesis of Ag Nanocubes and Au Nanocages. *Nat. Protoc.* **2007**, *2*, 2182–2190.

30. Hu, M.; Chen, J.; Li, Z.-Y.; Au, L.; Hartland, G. V.; Li, X.; Marquez, M.; Xia, Y. Gold Nanostructures: Engineering Their Plasmonic Properties for Biomedical Applications. *Chem. Soc. Rev.* **2006**, *35*, 1084–1094.

31. Cho, E. C.; Kim, C.; Zhou, F.; Cobley, C. M.; Song, K. H.; Chen, J.; Li, Z.-Y.; Wang, L. V.; Xia, Y. Measuring the Optical Absorption Cross Sections of Au−Ag Nanocages and Au Nanorods by Photoacoustic Imaging. *J. Phys. Chem. C* **2009**, *113*, 9023–9028.

32. Rycenga, M.; Wang, Z.; Gordon, E.; Cobley, C. M.; Schwartz, A. G.; Lo, C. S.; Xia, Y. Probing the Photothermal Effect of Gold-Based Nanocages with Surface-Enhanced Raman Scattering (SERS). *Angew. Chem., Int. Ed.* **2009**, *48*, 9924–9927.

33. Yavuz, M. S.; Cheng, Y.; Chen, J.; Cobley, C. M.; Zhang, Q.; Rycenga, M.; Xie, J.; Kim, C.; Song, K. H.; Schwartz, A. G.; *et al.* Gold Nanocages Covered by Smart Polymers for Controlled Release with Near-Infrared Light. *Nat. Mater.* **2009**, *8*, 935–939.

34. Moon, G. D.; Choi, S.-W.; Cai, X.; Li, W.; Cho, E. C.; Jeong, U.; Wang, L. V.; Xia, Y. A New Theranostic System Based on Gold Nanocages and Phase-Change Materials with Unique Features for Photoacoustic Imaging and Controlled Release. *J. Am. Chem. Soc.* **2011**, *133*, 4762–4765.

35. Wang, Y.; Liu, Y.; Luehmann, H.; Xia, X.; Brown, P.; Jarreau, C.; Welch, M.; Xia, Y. Evaluating the Pharmacokinetics and *In Vivo* Cancer Targeting Capability of Au Nanocages by Positron Emission Tomography Imaging. *ACS Nano* **2012**, *6*, 5880–5888.

36. Black, K. C. L.; Wang, Y.; Luehmann, H. P.; Cai, X.; Xing, W.; Pang, B.; Zhao, Y.; Cutler, C. S.; Wang, L. V.; Liu, Y.; *et al.* Radioactive ^{198}Au-Doped Nanostructures with Different Shapes for *In Vivo* Analyses of Their Biodistribution, Tumor Uptake, and Intratumoral Distribution. *ACS Nano* **2014**, *8*, 4385–4394.

37. Moghimi, S. M.; Hunter, A. C.; Murray, J. C. Long-Circulating and Target-Specific Nanoparticles: Theory to Practice. *Pharmacol. Rev.* **2001**, *53*, 283–318.

38. Peer, D.; Karp, J. M.; Hong, S.; Farokhzad, O. C.; Margalit, R.; Langer, R. Nanocarriers as an Emerging Platform for Cancer Therapy. *Nat. Nanotechnol.* **2007**, *2*, 751–760.

39. Davis, M. E.; Chen, Z.; Shin, D. M. Nanoparticle Therapeutics: An Emerging Treatment Modality for Cancer. *Nat. Rev. Drug Discovery* **2008**, *7*, 771–782.

40. Jokerst, J. V.; Lobovkina, T.; Zare, R. N.; Gambhir, S. S. Nanoparticle PEGylation for Imaging and Therapy. *Nanomedicine* **2011**, *6*, 715–728.

41. Hu, C.-M. J.; Fang, R. H.; Zhang, L. Erythrocyte-Inspired Delivery Systems. *Adv. Healthcare Mater.* **2012**, *1*, 537–547.

42. Knop, K.; Hoogenboom, R.; Fischer, D.; Schubert, U. S. Poly(ethylene glycol) in Drug Delivery: *Pros* and *Cons* as Well as Potential Alternatives. *Angew. Chem., Int. Ed.* **2010**, *49*, 6288–6308.

43. Hu, C.-M. J.; Zhang, L.; Aryal, S.; Cheung, C.; Fang, R. H.; Zhang, L. Erythrocyte Membrane-Camouflaged Polymeric Nanoparticles as a Biomimetic Delivery Platform. *Proc. Natl. Acad. Sci. U. S. A.* **2011**, *108*, 10980–10985.

44. Oldenborg, P.-A.; Zheleznyak, A.; Fang, Y.-F.; Lagenaur, C. F.; Gresham, H. D.; Lindberg, F. P. Role of CD47 as a Marker of Self on Red Blood Cells. *Science* **2000**, *288*, 2051–2054.

45. Durocher, J.; Payne, R.; Conrad, M. Role of Sialic Acid in Erythrocyte Survival. *Blood* **1975**, *45*, 11–20.

46. Hu, C.-M. J.; Fang, R. H.; Luk, B. T.; Chen, K. N. H.; Carpenter, C.; Gao, W.; Zhang, K.; Zhang, L. 'Marker-of-Self' Functionalization of Nanoscale Particles through a Top-Down Cellular Membrane Coating Approach. *Nanoscale* **2013**, *5*, 2664–2668.

47. Luk, B. T.; Hu, C.-M. J.; Fang, R. H.; Dehaini, D.; Carpenter, C.; Gao, W.; Zhang, L. Interfacial Interactions between Natural RBC Membranes and Synthetic Polymeric Nanoparticles. *Nanoscale* **2014**, *6*, 2730–2737.

48. Gao, W.; Hu, C.-M. J.; Fang, R. H.; Luk, B. T.; Su, J.; Zhang, L. Surface Functionalization of Gold Nanoparticles with Red Blood Cell Membranes. *Adv. Mater.* **2013**, *25*, 3549–3553.

49. Fang, R. H.; Hu, C.-M. J.; Chen, K. N. H.; Luk, B. T.; Carpenter, C. W.; Gao, W.; Li, S.; Zhang, D.-E.; Lu, W.; Zhang, L. Lipid-Insertion Enables Targeting Functionalization of Erythrocyte Membrane-Cloaked Nanoparticles. *Nanoscale* **2013**, *5*, 8884–8888.

50. Hochmuth, R.; Evans, C.; Wiles, H.; McCown, J. Mechanical Measurement of Red Cell Membrane Thickness. *Science* **1983**, *220*, 101–102.

51. Landry, J.; Samson, S.; Chrétien, P. Hyperthermia-Induced Cell Death, Thermotolerance, and Heat Shock Proteins in Normal, Respiration-Deficient, and Glycolysis-Deficient Chinese Hamster Cells. *Cancer Res.* **1986**, *46*, 324–327.

52. Svaasand, L. O.; Gomer, C. J.; Morinelli, E. On the Physical Rationale of Laser Induced Hyperthermia. *Laser Med. Sci.* **1990**, *5*, 121–128.

53. Hildebrandt, B.; Wust, P.; Ahlers, O.; Dieing, A.; Sreenivasa, G.; Kerner, T.; Felix, R.; Riess, H. The Cellular and Molecular Basis of Hyperthermia. *Crit. Rev. Oncol. Hematol.* **2002**, *43*, 33–56.

54. Cho, E. C.; Au, L.; Zhang, Q.; Xia, Y. The Effects of Size, Shape, and Surface Functional Group of Gold Nanostructures on Their Adsorption and Internalization by Cells. *Small* **2010**, *6*, 517–522.

55. Cho, E. C.; Xie, J.; Wurm, P. A.; Xia, Y. Understanding the Role of Surface Charges in Cellular Adsorption *versus* Internalization by Selectively Removing Gold Nanoparticles on the Cell Surface with a I_2/KI Etchant. *Nano Lett.* **2009**, *9*, 1080–1084.

56. Gratton, S. E. A.; Pohlhaus, P. D.; Lee, J.; Guo, J.; Cho, M. J.; DeSimone, J. M. Nanofabricated Particles for Engineered Drug Therapies: A Preliminary Biodistribution Study of PRINT Nanoparticles. *J. Controlled Release* **2007**, *121*, 10–18.

57. Peracchia, M. T.; Fattal, E.; Desmaële, D.; Besnard, M.; Noël, J. P.; Gomis, J. M.; Appel, M.; d'Angelo, J.; Couvreur, P. Stealth PEGylated Polycyanoacrylate Nanoparticles for Intravenous Administration and Splenic Targeting. *J. Controlled Release* **1999**, *60*, 121–128.

58. Maeda, H.; Wu, J.; Sawa, T.; Matsumura, Y.; Hori, K. Tumor Vascular Permeability and the EPR Effect in Macromolecular Therapeutics: A Review. *J. Controlled Release* **2000**, *65*, 271–284.